Lab on a Chip

A minimal constraint device for imaging nuclei in live Drosophila contractile larval muscles reveals novel nuclear mechanical dynamics

Journal:	*Lab on a Chip*
Manuscript ID	LC-ART-03-2020-000214.R1
Article Type:	Paper
Date Submitted by the Author:	09-Apr-2020
Complete List of Authors:	Lorber, Dana; Weizmann Institute of Science, Molecular Genetics Rotkopf, Ron; Weizmann Institute of Science, 2- Life Science Core Facilities, Bioinformatics unit Volk, Talila; Weizmann Institute of Science, Molecular Genetics

SCHOLARONE™
Manuscripts

A minimal constraint device for imaging nuclei in live *Drosophila* contractile larval muscles reveals novel nuclear mechanical dynamics

Dana Lorber[1], Ron Rotkopf[2], Talila Volk*[1]

1- Department of Molecular Genetics, Weizmann Institute of Science

2- Life Science Core Facilities, Bioinformatics unit, Weizmann Institute of Science

* Author for correspondence

Abstract

Muscle contractions produce reiterated cytoplasmic mechanical variations, which potentially influence nuclear mechanotransduction, however information regarding the dynamics of muscle nuclei (myonuclei) in the course of muscle contraction is still missing. Towards that end, a minimal constraint device was designed in which intact live *Drosophila* larva is imaged, while its muscles still contract. The device is placed under spinning disc confocal microscope enabling imaging of fluorescently labeled sarcomeres and nuclei during muscle contraction, without any external stimulation. As a proof of principle we studied myonuclei dynamics in wild-type, as well as in *Nesprin/klar* mutant larvae lacking proper nuclear-cytoskeletal connections. Myonuclei in control larvae exhibited comparable dynamics in the course of multiple contractile events, independent of their position along the muscle fiber. In contrast, myonuclei of mutant larvae displayed differential dynamics at distinct positions along individual myofibers. Moreover, we identified a linear link between myonuclear volume and its acceleration values during muscle contraction which, in *Nesprin/klar* mutants exhibited an opposite tendency relative to control. Estimation of the drag force applied on individual myonuclei revealed that force fluctuations in time, but not the average force, differed significantly between control and *Nesprin/klar* mutant, and were considerably higher in the mutant myonuclei. Taken together these results imply significant alterations in the mechanical dynamics of individual myonuclei in the Nesprin/*klar* myonuclei relative to control. Such differences provide novel mechanical insight into *Nesprin* function in contractile muscles, and might reveal the mechanical basis underlying *Nesprin*-related human diseases.

Introduction

Muscles are particularly receptive to mechanical stimulation and respond to increased mechanical load by changing transcriptional and translational levels (Egan and Zierath, 2013; Hawley et al., 2014). Recent evidence suggests that the nuclear envelope transmits mechanical cues into the nucleus, which are essential to control epigenetic state and gene expression (Fedorchak et al., 2014; Martins et al., 2012). However, the way such mechanical signals spread over hundreds of myonuclei comprising individual myofibers remains to be elucidated (Hector et al., 2015; Rindom and Vissing, 2016). To reveal the mechanical dynamics of myonuclei during muscle contraction it is essential to accumulate quantitative information during the course of contractile events. Obtaining such information in an intact live organism is challenging due to the difficulty to follow the path of individual myonuclei within myofibers in a single contractile event.

Cytoplasmic mechanical signals are transmitted to the nucleus mainly via the Linker of Nucleoskeleton and Cytoskeleton (LINC) complex (Lombardi and Lammerding, 2015; Rothballer and Kutay, 2013). This evolutionarily conserved complex (Razafsky 2014, Mellad et al., 2011) is comprised of cytoskeletal-associated Nesprins, proteins that contain **K**larsicht, **A**NC-1, **S**yne **H**omology (KASH) domain. Nesprins directly bind to **S**ad1p, **UN**C-84 (SUN) domain proteins at the perinuclear space, thereby forming a link between the cytoskeleton and the nucleoskeleton (Cartwright and Karakesisoglou, 2014; Mellad et al., 2011). Previous studies indicated the essential contribution of the LINC complex to nuclear morphology (Banerjee et al., 2014; Rothballer and Kutay, 2013), nuclear migration and positioning (Bone et al., 2014; Rajgor and Shanahan, 2013; Stroud et al., 2017), regulation of nuclear lamina proteins, and chromatin organization (Mellad et al., 2011a; Osmanagic-Myers et al., 2015; Rothballer and Kutay, 2013).

Vertebrate muscles express multiple LINC complex genes, impeding functional analysis of the complex. The *Drosophila* genome contains only two KASH encoding genes, namely *klarsicht* (*klar*) (Xie and Fischer, 2008) and *Msp300* (Elhanany-Tamir et al., 2012; Xie and Fischer, 2008; Zhang et al., 2002)), and a single SUN encoding gene, *klaroid* (*koi*) (Kracklauer et al., 2007), which facilitates dissecting their functional contribution. Previous analyses indicated that in muscles, *Msp300/Nesprin* is essential for nuclear positioning through mediating association of the nuclear membrane with *Drosophila* Titin (DTitin) at the Z-discs (Elhanany-Tamir et al., 2012). Furthermore, Klar and Msp300 mediate connection of the microtubule

network with the nuclear membrane (Elhanany-Tamir et al., 2012; Wang et al., 2015). In addition to nuclear position defects, LINC complex mutant myonuclei exhibited differential nuclear size, variable DNA content, and dysregulated DNA replication (endoreplication). The variability in DNA content in myonuclei of single myofibers implied a novel function of the LINC complex, namely in equalizing the degree of DNA endoreplication among numerous myonuclei of individual myofibers (Wang et al., 2018).

Despite the wide tissue distribution of the LINC complex, mutations in the genes coding for its various components lead primarily to defects in force generating tissues such as skeletal muscles and cardiomyocytes, implying its unique functional contribution in these tissues. To study myonuclear dynamics during muscle contraction, we developed a device that allows imaging of larval body wall muscles in live intact larvae. Unlike other experimental systems, our approach does not require muscle isolation (Barash et al., 2005; Drost et al., 2003; Eldred et al., 2010; Hakim et al., 2013), use of anesthetized organism (Kakanj et al., 2019; Zhang et al., 2010), immobilization of the model (Chaudhury et al., 2017; Dexter et al., 2014; Ghaemi et al., 2015; Mondal et al., 2012; Wolf et al., 2015; Zhang et al., 2016), or a combination of both methods (Csordás et al., 2014; Sloboda et al., 2013; Wolf et al., 2015) and thus allows to record and estimate nuclear dynamics in intact live organisms.

Significantly, we found substantial differences in the spatiotemporal dynamics of *Nesprin/klar* mutant myonuclei relative to control along the muscle fiber during muscle contraction. Our results suggest that in contrast to control muscles, where synchronized myonuclear dynamics along the entire muscle fiber is maintained in the course of muscle contraction, Nesprin/*klar* mutant myonuclei lack such synchronization and uniformity. We assume that myonuclear dynamics during muscle contraction correlates with the net forces acting on the nucleus, derived mainly from viscous drag force (Forgacs and Newman, 2005). Thus, the differences between the dynamics of the control and mutant nuclei during contraction may result from different forces applied on the myonuclei during contraction.

Materials and Methods

Design of the minimal constraint device

Aiming to design a device for imaging active muscles in their intrinsic environment, a minimal constraint device was constructed enabling visualization of muscles and nuclei in an intact live *Drosophila* 3rd instar larvae. The fundamental guideline for the system design was to create a device that entails minimal intervention of muscle physiology and in addition allows spontaneous muscle contractions which then can imaged in high magnification under the microscope.

The larva is placed in a groove, and glass capillaries are glued to both head and tail edges, as shown in Figure 1A and Figure 1B. Then, the larva is coated with hydrogel, topped with a glass coverslip and the entire system is inverted, and placed on the microscope stage.

The device consists of an aluminum base that holds all the parts of the apparatus together, which after the assembly of the device, is placed on the microscope stage. A high precision coverslip glass, 50 mm long, 24 mm wide and 170 μm thickness (Cat. # 0107222, thickness No. 1.5H, Pauk Marienfeld GmbH&Co.KG) is placed in the aluminum base in its corresponding frame in the center of the device, and is held with 4 rubber stoppers, 12.2 mm long and 4.1 mm in diameter, as shown in Figure 1C. A Teflon™ frame with two hinges on either side is placed on top of the cover glass with its groove facing to the glass.

First, a bar made of *Delrin*® (DuPont) with a lengthwise groove of 740x740 μm is inserted into the frame. The groove, which is extended through both the bar and frame, was designed for correct alignment of the larva with its attached capillaries during adhesion, and for preventing larval bending during spontaneous contractions. The length of the central bar is 20.8 mm and the length of the Teflon frame is 44.9 mm from side to side, which is long enough to support the weight of the capillaries. The dimensions of the groove allow its rotation to the correct position using a fine brush. At a later stage, this bar is replaced with a Teflon bar with a 1000 μm wide and 820 μm deep groove, that allows wider space for larval contraction. Teflon and Delrin were chosen as the materials for the bars and frame since they are inert both to the larvae and to the glue so if some glue drops on the device parts during the assembly of the system it does not affix the parts.

The glass capillaries (Drummond Scientific Company, PA, USA, cat. #1-000-0010, O.D 0.026", I. D. 0.0078") are glued to the larval head and tail by Cyanoacrylates (Superglue liquid, Pattex,

Australia). In order to make the handling of the capillaries easier during assembly, a plastic bead was attached to one tip of each capillary by applying adhesive on the outer side of the capillary so that the glue will not clog the capillary.

The larva is coated with hydrogel to fill the gaps between the bar and damp larval movement however it is soft enough to allow spontaneous muscle contractions, and in addition it keeps the larvae in a moist environment during the experiment. The hydrogel used was alginate, a common material in the drug and food industry (Olatunji, 2015; Wan et al., 2009), that polymerizes instantaneously at room temperature in the presence of bivalent cations. In these experiments, a solution of 4% alginate (cat. # 180947, Aldrich) dissolved in 0.9% saline (NaCl, cat. # 0277, J. T. Baker) was polymerized with a solution of 0.8M of $CaCl_2 \cdot 2H_2O$ (cat. # 2382.0.0500, Merck).

Assembly of the minimal constraint device

Third instar *Drosophila* larva was placed in a small drop of water and temporally anesthetized by blowing CO_2 into the water. This step is necessary to allow accurate positioning of the larva in the device and its gluing to the capillaries. The anesthesia dissipates within a few minutes, before the experiment begins.

Under a binocular microscope, the larvae is inserted to the groove of the Delrin bar, which is placed inside the Teflon frame, and then rotated with a fine brush along its axis so that the longitude muscles will face the coverslip glass.

A capillary is filled with adhesive glue using its capillary force by dipping it into a drop of glue for a few seconds. The capillary outer walls are wiped from glue and then it is gently pushed along the groove until it touches the larval posterior end. A second capillary is used in the same manner to attach the head.

Next, the base of the device, with the cover glass secured with the rubber stoppers facing down, is placed on top of the Teflon frame with the larva and all parts inverted back so the rubber tubes are now facing up.

At this stage, the Delrin bar is replaced with a Teflon bar with a wider groove. The narrow groove is important for accurate adhesion of the capillaries along the axis of the larval body

while the Teflon bar with the wider groove allows more freedom in the movement of the larva. After removing the *Delrin* bar, 14µl of the calcium chloride solution (see above) are added on top of the larva and the capillaries ends, (at the point of their attachment to the larvae). The groove of the Teflon bar is filled with 22 µl alginate solution, and is immediately inserted into the frame and gently pressed for 10 seconds to allow polymerization. To assure that all the alginate solution is polymerized, 22 µl of calcium chloride solution is added on both sides of the Teflon bar. At this stage, the larvae usually starts to recover from the anesthesia and imaging can begin. (See images of the assembly process in supplementary material, Figure S1).

Flies

The flies used in this study, P{UAS-mCherry.NLS}2 and P{GAL4-Mef2.R}2, were obtained from Bloomington Stock Centre. The flies were recombined on the second chromosome and crossed with flies with endogenously EGFP-tagged *sallimus* (obtained from Belinda Bullard, Department of Biology, University of York). For the analysis of *klar* homozygous larvae, the $klar^{1\text{-}18}$*/TM6,Tb* allele, which lacks all *klar* coding exons (obtained from Michael Welte, Department of Biology, University of Rochester) was recombined with the Sls-GFP insertion, and the recombined line P{UAS-mCherry.NLS}2, P{GAL4-Mef2.R}2 was combined with $klar^{1\text{-}18}$*/TM6,Tb*.

Imaging

All the experiments were performed with a VisiScope CSU-W1 Spinning Disk Confocal Microscope (Visitron Systems, Puchheim, Germany) based on an Olympus IX83 inverted microscope, a Yokogawa CSU-W1 scan head, and a PCO Edge4.2 sCMOS camera. The images were acquired with a 20X air objective (NA=0.75), which enables visualization of an entire intact longitudinal muscle during its activity.

Laser lines of 561 nm and 488 nm were used to excite the mCherry and GFP fluorescent markers, respectively, and the exposure time of each image was 20 ms. In order to shorten the time between acquisitions of consecutive images, an emission dual band filter (cat. # 59022m, Chroma Technology Corp, USA) was added to the microscope, which isolates the emitted light to two separate monochromatic wave lengths. The merged images of the myonuclei and sarcomeres were used to find the edges of the muscles and to determine which myonuclei belong

to the tested muscle. Spontaneous muscle contractions were recorded continuously, up to 500 pairs of images in a single sampling, which is the limitation of the sampling system.

For quantification, only full muscle contractions were considered. Contraction onset and completion were determined when at least in two consecutive images the nuclei did not change their position relative to each other.

Quantification of myonuclear dynamics

To determine the spatiotemporal dynamics of each nucleus along the muscle fiber during a contractile event, its displacement in time was measured. The location of each nucleus in each image, throughout a single contractile event, was measured using the manual tracking plug-in from ImageJ. The displacement d of a nucleus that occurred between two successive sampling times t_1 and t_2 was determined as follows:

$$d = \sqrt{(x_2 - x_1)^2 + (y_2 - y_1)^2}$$

where (x_1, y_1) is the location of the middle of the nucleus at t_1 and (x_2, y_2) is the location at t_2, as shown in Figure 2A. The displacement function in time was obtained from measurements over multiple sampling time points in the system.

At the end of each contraction, the muscle returned to its original position. Hence, the displacement measurements relate to a stationary frame of reference and there is no need to correct for relative movement of the larva and device.

To calculate the velocity in time v(t) and acceleration in time a(t), the first and second discrete numerical central derivatives with unevenly spaced points were calculated, respectively, based on Taylor's expansion (Gupta, 2015). This approach was used because the sampling rate of the microscope was found to be inconsistent. Figure 2B-D shows a representative example of the three functions in time, as calculated for a single nucleus in a single contraction. Based on these three functions in time, several physical parameters were calculated, such as average velocity and average acceleration during contraction. We also calculated the path, which is the trajectory length of a nucleus during contraction, and the net displacement, which is the distance from the starting location to the end one.

For low Reynolds' number (Re<1), the viscous drag force F on a spherical body of radius R moving in the fluid can be calculated using Stokes law: $F=6\pi\eta Rv$, where η is the viscosity of the fluid and v is its velocity. (Fuks NA, 1964). The force time derivative dF/dt, assuming the viscosity of the fluid and the geometry of the body are constant, yields:

$$\frac{dF}{dt} = 6\pi\eta R\frac{dv}{dt} = 6\pi\eta Ra$$

where a is the acceleration of the sphere.

To calculate the drag force applied on an oblate axisymmetric ellipsoid moving in a fluid, a geometric correction factor k is introduced to Stokes law: $F=6\pi\eta rvk$, where r is the equatorial radius of the ellipsoid. k is dependent on the ratio β, between r and other axis of ellipsoid b, and on the direction of the flow in relation to the axis of revolution. When the flow is perpendicular to b (Fuks NA, 1964), then:

$$k = \frac{\frac{8}{3}(\beta^2-1)}{\left(\frac{\beta(3\beta^2-2)}{\sqrt{\beta^2-1}}arctan\left(\sqrt{\beta^2-1}\right)\right)-\beta}$$

To estimate the average height of control and *klar* mutant nuclei, in another set of experiments, larvae were tilted to allow visualization of the nuclear and muscle sagittal plane, enabling imaging of the nuclear height at high resolution. Imaging conditions were as described previously. Using the modified Stokes equation allows to estimate the average force (AF) and average force time derivative (AFTD) applied on the myonuclei during contraction.

Programming

A Perl script was used to read the values from the Excel worksheet and then to perform the required functions. The output was written to a new worksheet.

Statistics

When one average value was used per larva, differences between WT and mutant larvae were tested using *t*-tests. Differences accounting for location (anterior vs. middle vs. posterior) were analyzed using a repeated-measures ANOVA, accounting for the random effect of each larva, i.e. one model including the group effect (control vs. mutant), and two models for each group separately. Contrasts within a certain location were tested using *t*-tests. Variance comparisons were done using *F*-tests. All statistical analyses were done using R v. 3.5.1.

Effect size of average velocity between locations was estimated using Cohen's D.

To test the effect of various mechanical parameters on nuclear size, a linear mixed effects model was used, with genotype and the measured parameter as fixed effects, and a random intercept and slope per larva. Statistics were calculated using R (v. 3.6.0), and the packages 'lme4' and 'lmerTest'.

Results

The minimal constraint device for imaging live intact Drosophila larvae

To record myonuclear dynamics during muscle contractile events, we developed a device that enables tracking myonuclei in muscles of intact, live 3rd instar *Drosophila* larvae under a spinning disc microscope (see Materials and Methods). The myonuclei were labelled with mCherry fused to a nuclear localization signal (mCherry-NLS) driven by *mef2-GAL4* driver, and sarcomeres were visualized by endogenous GFP insertion into the *D-Titin* gene (*sallimus-GFP*). Longitudinal muscles were routinely recorded using a 20X objective, capturing a length of 665.6 μm, enabling image acquisition of an entire myofiber from anterior to posterior segmental borders (representative movies 1 and 2 of control and *klar* mutant are shown in Supplementary information).

To evaluate the dynamic behaviour of the myonuclei in the course of a single contractile event, we calculated the displacement in time of each nucleus based on the change in its x-y position from frame to frame. This was followed by calculating the velocity and acceleration for each of the myonuclei in numerous movies taken. A representative example for the displacement of a few myonuclei that occurred between two consecutive images is shown in Figure 2A, in which the colour of myonuclei was artificially changed from red (earlier point) to green (later

point, t=82 ms). Note that the displacements (d) of these myonuclei are not uniform during this time interval. A representative example of the displacement of a single myonucleus in time during full contraction is shown in Figure 2B, and its velocity and acceleration values are shown in Figure 2C and 2D, respectively . Note that in this example, nuclear displacement increased rapidly in the first 800 ms and then tapered off. Nuclear velocity decreased with time, and the absolute values of nuclear acceleration varied in time.

Representative single still images of relaxed or fully contractile myofibers of control larvae are shown in Figure 3A-D. To follow nuclear dynamics in a LINC complex representative mutant, we used *Nesprin/klar* homozygous larvae in combination with the fluorescent markers described above. Representative single confocal still images of relaxed or fully contractile myofibers of *Nesprin/klar* homozygous mutant muscles, are shown in Figure 3E-H. Consistent with previous studies, the *Nesprin/klar* mutant muscles displayed uneven distribution of the myonuclei and, in addition, exhibited variable size (Figure 3E-H). The trajectories of each of the nuclei shown in Figure3A-H are diagrammed in Figure 4A-B (A for control and B for *Nesprin/klar* mutant muscles). Notably, differential displacement of myonuclei was observed in control and *Nesprin/klar* mutant muscles. These results suggest that the dynamics of the *klar* mutant myonuclei differs from that of control.

Quantitative analysis of myonuclear dynamics of control and Nesprin/klar mutant muscles

To reveal whether nuclear dynamics during muscle contraction of *Nesprin/klar* mutant myonuclei differs from that of control, we calculated the time dependent displacement, velocity, and acceleration of myonuclei in numerous contractile events in control and *Nesprin/klar* mutant larvae. In both groups (control or *Nesprin/klar* mutant), measurements of nuclear displacements were taken from five 3rd instar larvae, in which up to 10 events of muscle contractions were quantified from a single muscle, and for all visible myonuclei. Table 1 summarizes the number of myonuclei analysed for each muscle, and the number of contractile events analysed for each group.

Exp.	**Num. of nuclei**	**Num. of contractions**	**Exp.**	**Num. of nuclei**	**Num. of contractions**
Control 1	15	6	***Klar* 1**	6	7
Control 2	9	8	***Klar* 2**	17	7

Control 3	11	7	***Klar* 3**	7	6
Control 4	12	7	***Klar* 4**	9	10
Control 5	13	10	***Klar* 5**	13	8
sum	**60**	**38**	**sum**	**52**	**38**

Table 1: Summary of the number of nuclei analysed

The quantified mechanical parameters included contraction time (Figure 5A), path (Figure 5B), average velocity (Figure 5C and 5D), and average acceleration (Figure 5E and 5F).

The average duration of a single contractile event in control larvae was significantly longer compared to that of *Nesprin/klar* mutant muscle (1286 ± 372 ms compared to 715 ± 246 ms, *t*-test, p=0.024). Then, the path that each myonucleus traversed during a single contractile event was measured by the summation of all displacements that occurred between consecutive sampling points during contraction. Each point in Figure 5B represents the average path of all the myonuclei from one muscle of a single larva, calculated from 6 to 17 myonuclei that underwent 6 to 10 contractile events, so that each point represents the average of corresponding 42 to 130 different values. The results indicated that the average path traversed by control myonuclei in an individual contractile event was significantly larger relative to that of *Nesprin/klar* myonuclei (51 ± 10 μm relative to 29 ± 5 μm, *t*-test, p=0.005). A similar tendency was observed when comparing the displacement of the myonuclei between control and *Nesprin/klar* mutant muscles (not shown). Taken together, these results indicate a significant difference between the extent of muscle contraction in *Nesprin/klar* versus control muscles.

Next, the average velocity during contraction was calculated for control and *Nesprin/klar* myonuclei per larva (Figure 5C). No significant difference between control and *Nesprin/klar* mutant groups was observed (*t*-test, p=0.7). Further analysis addressed nuclear dynamics at distinct locations along myofibers. The two myonuclei closest to the anterior segmental border were defined as “anterior” myonuclei, those closest to the posterior segmental border were defined as “posterior” myonuclei, and the two myonuclei at the geometric center of the myofiber were defined as “middle” myonuclei. Figure 5D shows that the velocity in *Nesprin/klar* mutant changes significantly along the myofiber (p=0.032), primarily because the average velocity of

the posterior myonuclei significantly differed from myonuclei at the anterior and middle positions. (effect size: Cohen's D =1.55). The difference between the average velocity values in the distinct positions of the control nuclei was less pronounced. While a repeated-measures ANOVA showed that the average velocity did not change significantly along the fiber (p=0.065), the effect size showed a large difference in the values between the anterior and middle pats of the fiber (effect size=0.88). Notably, the average velocity of posterior *Nesprin/klar* mutant myonuclei was higher than that of corresponding control myonuclei (p=0.012) (Figure 5D).

Further calculation of the acceleration values of all the myonuclei during all the contractions indicated that *Nesprin/klar* mutant myonuclei exhibited higher absolute average acceleration values relative to control (p=0.034) (Figure 5E). In control myonuclei, the average acceleration was $-3.14\cdot10^{-5}\pm2.42\cdot10^{-5}$ μm/msec^2, and in *Nesprin/klar* myonuclei it was $-1.39\cdot10^{-4}\pm7.8\cdot10^{-5}$ μm/msec^2, an order of magnitude higher. Note that in this case, negative acceleration values represent a decrease in velocity rather than direction of movement. Notably, the variance of the average acceleration values was significantly higher in the *Nesprin/klar* mutant muscles (p=0.044). Normalization of the acceleration variance with the average acceleration ($\text{variance}^{\text{acceleration}}/\text{average}^{\text{acceleration}}$) indicated that in control this value was -1.86E-05, whereas in *klar* mutant it was -4.38E05. This demonstrates a 2.35 fold increase of the normalized variance in the mutant, indicating that the higher variance in nuclei acceleration could not be explained just by the higher acceleration values in the mutant. Moreover, whereas the average myonuclear acceleration during contraction in control myofibers was uniform at distinct positions along the myofibers (p=0.39) (Figure 5F), in *Nesprin/klar* mutant myofibers, this homogeneity was lost and the average myonuclear acceleration values differed, primarily due to an increase in acceleration of the posterior mutant myonuclei (p=0.025) (Figure 5F). A significant difference in the average acceleration values between control and *Nesprin/klar* mutant was also noted at the posterior position (p=0.009) (Figure 5F).

In summary, our analysis of nuclear mechanics during muscle contraction indicates that control myonuclei appear to be exposed to homogenous mechanical dynamics, whereas the *Nesprin/klar* mutant myonuclei experience variable mechanical dynamics, indicated by the differential velocity and acceleration values along the fiber during muscle contraction.

Nuclear dynamics might be primarily influenced by the variable size of myonuclei observed in *Nesprin/klar* mutant muscles (Elhanany-Tamir et al., 2012). To address a possible link between nuclear volume and nuclear mechanics, we first calculated nuclear volume of each of the myonuclei. Calculation was based on the nuclear ellipsoid shape, with a volume V equals $V = \frac{\pi}{6}LWH$, where L is the length of the nucleus, W represents its width, and H is its height (Webster and Eren, 2018). To estimate the average height of control and *Nesprin/klar* mutant nuclei, larvae were tilted to allow visualization of the nuclear and muscle sagittal plane. Visualization of the nuclear height at high resolution enabled its precise measuring. These measurements indicated that the average height of myonuclei was 6.96 μm for control, and 6.85μm for *klar* mutant myonuclei (a difference which is not statistically significant). We then plotted nuclear volume against the average acceleration for each of the myonuclei (Figure 6). The calculated slopes for control and *Nesprin/klar* mutant showed opposing tendencies. While for the control myonuclei increased nuclear volume correlated with decreased average acceleration, in *Nesprin/klar* mutant myonuclei, the increased nuclear volume correlated with increased average acceleration (interaction p= 0.007). Interestingly, when plotting nuclear volume against the average velocity the difference between the groups was not conclusive (interaction p= 0.06) (Figure S2). Taken together these results suggest that whereas in both control and *Nesprin/klar* groups myonuclear volume is tightly linked to the average acceleration values, they respond in opposing trends, indicating a significant difference in their reaction to muscle contraction.

Estimation of the average force and its time derivative applied on the myonuclei during contraction

To estimate the average drag force (AF) exerted on the myonuclei during contraction, we used Stokes law (see Materials and Methods). The viscosity value used to calculate the AF was chosen on the basis of results obtained from several studies that measured human muscle viscosity *in vivo* (Chakouch et al., 2016; Debernard et al., 2013; Gennisson et al., 2010; Hoyt et al., 2008). These calculations displayed a range of 0.7 Pa·s to 10.6 Pa·s for relaxed muscles and 11.6 Pa·s to 12.6 Pa·s for different levels of contractions and loads. We chose a value of 10 Pa·s, which reflects the average value of the viscosity between relaxed and contractile muscle *in vivo*.

No significant difference was observed between the AF applied on myonuclei during contraction of control or *Nesprin/klar* myonuclei (Figure 7A), (*t*-test, p=0.73). Significantly, however, we observed a substantial difference between the Average Force Time Derivative (AFTD) obtained for myonuclei in control versus *Nesprin/klar* myonuclei (Figure 7B). On average, *Nesprin/klar* mutant myonuclei were found to be subjected to higher absolute values of AFTD relative to control (p=0.033), with an order of magnitude higher variance (p=0.048). Furthermore, AFTD values differed for myonuclei at different positions along the myofiber in *Nesprin/klar* mutant muscles (p=0.00165), whereas control myonuclei showed uniformity along the myofiber (p=0.3) (Figure 7C).

Consistent with the differences obtained when plotting nuclear volume against average acceleration (Figure 6A), we found that the dependence between nuclear volume and AFTD was significantly different between control and *Nesprin/klar* larvae (interaction p=0.029) (Figure 7D), and similarly indicated opposing tendencies. No significant difference was observed between the groups when plotting the volume against the AF (interaction p=0.112) (Figure S2). We assume that the average acceleration is influenced by the net mechanical environment of the myonuclei. Alterations in nuclear volume are linked to the net forces that the nuclei encounter during muscle contraction, and therefore might impact on both the acceleration, as well as drag forces. The tendencies described in Fig 6 as well as in Fig 7D imply that indeed the linkage between nuclear volume and either the average acceleration or the change in drag forces display opposite dependency. Taken together, these results suggest a link between the mechanical environment of a given myonucleus and its volume, which exhibits opposing trends in control relative to *Nesprin/klar* mutant myonuclei.

Discussion

In the present study we describe a minimal constraint device enabling visualization of nuclei dynamics in muscle fibers, during the course of muscle contraction in intact live model organism. This device is unique because it allows visualization of organelles (including nuclei) within the muscle cytoplasm during contractile/relaxation waves, without a need to anesthetize or deform the tissue. Importantly, the use of the device is not limited for the detection of nuclei

dynamics, and it allowed us to image the dynamics of various subcellular structures within the muscle cytoplasm in the course of muscle contraction. Such structures include buckling of the microtubule network, Ca++ flux into the muscle cytoplasm, chromatin deformation, and nuclear lamina indentations, all of which have been imaged during muscle contractile/relaxation waves (see movies 3-6 in Supplementary information).

The duration of a single muscle contraction and the corresponding parameters of the sampling system (speed of microscope camera combined with the system software) limited us to take a single optical section for each time frame. Since the nuclei are positioned on top of the sarcomeres, their focal plane differs from that of the sarcomeres, and therefore it is difficult to visualize the nuclei and the underlying sarcomeres simultaneously at the same frame. Consequently, in most of the movies in which nuclei were visible, sarcomeres imagining was insufficient, and therefore we were unable to detect sarcomeres shortening at the vicinity of the myonuclei.

Mechanical signals transduced across the nuclear membrane have been shown to be critical for regulation of the chromatin state, gene expression levels, and nuclear import of transcription factors (Cho et al., 2017; Elosegui-Artola et al., 2017; Fedorchak et al., 2014; Miroshnikova et al., 2017; Uhler and Shivashankar, 2017). Myonuclei are exposed to variable cytoplasmic mechanical inputs in the course of their contractile waves; however, quantitative information regarding the extent of the actual mechanical forces, as well as their spatial and temporal distribution along the elongated myofiber, in a living organism during spontaneous contractions, is still missing. Here, we provide such quantitative mechanical information regarding myonuclear dynamics at a single myofiber resolution in live organism. Importantly, the obtained nuclear dynamics data was compared to that of a LINC-representative mutant, *Nesprin*/*klar* and significant differences between the mechanical environment of myonuclei in the mutant myonuclei were identified.

A key conclusion from these experiments is that *Nesprin/klar*, shown previously to mediate nucleus-cytoskeleton interaction, is essential for equalizing the mechanical dynamics of the myonuclei and attenuates the drag forces applied on the nuclear membrane of each of the multiple myonuclei that consist a single myofiber. We suggest that providing the myonuclei with stable and homogenous mechanical dynamics facilitates their synchronized response to a large variety of physiological and mechanical conditions.

Overexpression of Cherry-NLS led to variations in nuclear volume both in control and *Nesprin/klar* mutant myonuclei. However, the dependence between myonuclei volume and the average acceleration exhibited opposing tendencies. We suggest that *Nesprin/klar* provides a functional link between myonuclear volume and its response to mechanical forces produced during muscle contraction.

Our study demonstrates that whereas control myonuclei experience comparable average velocity and acceleration values during contraction and, hence, uniform AF and AFTD, the *Nesprin/klar* mutant myonuclei fail to maintain this homogeneity. Lack of synchronization between the myonuclei observed in *Nesprin/klar* mutants is predicted to cause non-homogenous response to mechanical stimulation produced in the course of muscle contraction. Previous reports describe lack of nuclear size uniformity among myonuclei of *Nesprin*/*klar* mutant myonuclei in *Drosophila*, as well as in humans (Elhanany-Tamir et al., 2012; Puckelwartz et al., 2010; Stroud et al., 2017). Furthermore, we previously reported that *Drosophila* LINC complex-deficient myonuclei contain variable DNA content as a result of unsynchronized DNA replication (Wang et al., 2018). Variable size and DNA content in *LINC* mutant myonuclei correlates, and might be functionally related to the variable mechanical dynamics observed in the mutant myonuclei. The higher sensitivity of posterior myonuclei observed in *Nesprin/klar* mutant muscles might reflect differential mechanical dynamics in the posterior aspects of the myofiber. Such mechanical variations are presumably sequestered by nuclear association with the cytoskeleton via *Nesprin*/*klar*, and possibly other LINC complex components.

Our measurements indicated that the average contractile duration of the *Nesprin/klar* mutant muscles is significantly shorter than that of control muscles. However, since the average velocity of myonuclei did not differ between control and mutant groups, we suggest that the differential mechanical properties of the mutant myonuclei observed in the present study are not solely indirect consequence of the shorter contractile interval of the mutant muscles, but rather represent intrinsic differential mechanical properties of the mutant myonuclei. A partial explanation for the shorter contractile duration may be our previous finding that Troponin C levels decreased at the transcription, mRNA, and protein levels in *Nesprin/klar* mutants (Wang et al, 2018). Aberrant muscle contraction is a hallmark of human muscular dystrophies associated with mutations in the LINC complex (Janin et al., 2017; Méjat and Misteli, 2010).

The immediate surroundings of myonuclei include a network of microtubules, sarcoplasmic reticulum, multiple mitochondria and sarcomeres. During muscle contraction and sarcomere shortening, the myonuclei move with the sarcomeres. However, the cytoplasm does not move together with the sarcomeres, thus the nuclei are subjected to friction forces with the cytoplasm content. Based on this assumption, it was possible to give an approximation for the drag force applied on the myonuclei during their movement, using Stokes' law. Interestingly, although the AF values did not differ between control and *Nesprin/klar* mutant myonuclei, the AFTD and its variance during the contractile events were significantly higher in the *Nesprin/klar* myonuclei. Therefore, force fluctuations in time may represent the main difference between control and *Nesprin/klar* mutant muscles. Such force fluctuations might have long term effects on nuclear activity.

The average acceleration and hence, the AFTD during contraction of control myonuclei was an order of magnitude lower than that measured for the *Nesprin/klar* myonuclei. In addition the variance in the acceleration and AFTD values in control myonuclei was significantly lower than that of *Nesprin/klar* myonuclei. These differences might result from either abnormal muscle contractions, or directly due to impaired function of the LINC complex, or combination of both.

Nesprin-related human diseases including Emery-Dreifuss muscular dystrophy (EDMD), Dilated Cardiomyopathy (DCM), or Artrogryposis, all of which contain specific mutations in one of the Nesprin genes (Attali et al., 2009; Méjat and Misteli, 2010; Zhang et al., 2007), are characterized by severe impairment of skeletal or cardiac muscle function. Although the Nesprin genes are expressed in wide range of tissues, the muscle tissue is the most sensitive to these mutations. It has been hypothesized that the reason for muscle disfunction in Nesprin-related diseases lies on aberrant mechanical signals, transferred by Nesprin proteins into the nucleus. Furthermore, changes in the mechanical environment of the muscle nuclei have been postulated to affect epigenetic nuclear events, leading to impaired gene expression in the muscle tissue. Direct evidence for different mechanical dynamics of muscle nuclei in Nesprin mutants is still missing. Here, we demonstrate evidence implying that the nuclei of the Nesprin mutant muscles are indeed exposed to different mechanical environment relative to healthy control muscles, thus providing confirmation for the hypothesis regarding the function of the Nesprin genes in muscles.

In summary, our results suggest that the LINC complex buffers the nuclear envelope from variable mechanical perturbations that occur during muscle contraction and, thereby, provides a uniform and stable mechanical dynamics for all myonuclei within individual fibres, which is required for homogenous myonuclear response.

Acknowledgements

We thank the Bloomington Stock Centre for various fly lines, the Developmental Studies Hybridoma Bank (DSHB) for antibodies, and FlyBase for important genomic information. We are grateful for Samuel Safran, from the Department of Chemical and Biological Physics, Weizmann Institute of Science, and his students Dan Deviri and Ohad Cohen for insightful discussions and helpful remarks, Mike Shorkend for writing the codes for our analysis and Nitzan Konstantin for English editing. We thank Karen Fridman and Daria Amiad-Pavlov for helping us to broaden the performance of the device and apply it into additional experimental systems. This study was supported by a grant from the NSF-BSF (BSF application 2016738 to T.V. and NSF application 1715606 to JL) and ISF grant 750/17 (T.V.). FlyBase is supported by a grant from the National Human Genome Research Institute at the U.S. National Institutes of Health #U41 HG000739. Support is also provided by the British Medical Research Council (#MR/N030117/1) and the Indiana Genomics Initiative. The BDSC is supported by a grant from the Office of the Director of the National Institute of Health under Award Number P40OD018537. NIH ICs OD, NIGMS, NICHD and NINDS contribute to funding of this award.

Author contributions

D.L. conceptualized, investigated, performed formal analysis and wrote the original draft, R.R. performed formal analysis, T.V. supervised, provided funding, reviewed and edited the draft.

References

Anno T, Sakamoto N, Sato M. 2012. Role of nesprin-1 in nuclear deformation in endothelial cells under static and uniaxial stretching conditions. *Biochem Biophys Res Commun* **424**:94–99. doi:10.1016/j.bbrc.2012.06.073

Attali R, Warwar N, Israel A, Gurt I, McNally E, Puckelwartz M, Glick B, Nevo Y, Ben-Neriah Z, Melki J. 2009. Mutation of SYNE-1, encoding an essential component of the nuclear lamina, is responsible for autosomal recessive arthrogryposis. *Hum Mol Genet* **18**:3462–3469. doi:10.1093/hmg/ddp290

Banerjee I, Zhang J, Moore-Morris T, Pfeiffer E, Buchholz KS, Liu A, Ouyang K, Stroud MJ, Gerace L, Evans SM, McCulloch A, Chen J. 2014. Targeted Ablation of Nesprin 1 and

Nesprin 2 from Murine Myocardium Results in Cardiomyopathy, Altered Nuclear Morphology and Inhibition of the Biomechanical Gene Response. *PLoS Genet* **10**. doi:10.1371/journal.pgen.1004114

Barash IA, Mathew L, Lahey M, Greaser ML, Lieber RL. 2005. Muscle LIM protein plays both structural and functional roles in skeletal muscle. *Am J Physiol Cell Physiol* **289**:C1312-20. doi:10.1152/ajpcell.00117.2005

Bone CR, Tapley EC, Gorjanacz M, Starr DA. 2014. The Caenorhabditis elegans SUN protein UNC-84 interacts with lamin to transfer forces from the cytoplasm to the nucleoskeleton during nuclear migration. *Mol Biol Cell* **25**:2853–2865. doi:10.1091/mbc.E14-05-0971

Brosig M, Ferralli J, Gelman L, Chiquet M, Chiquet-Ehrismann R. 2010. Interfering with the connection between the nucleus and the cytoskeleton affects nuclear rotation, mechanotransduction and myogenesis. *Int J Biochem Cell Biol* **42**:1717–1728. doi:10.1016/j.biocel.2010.07.001

Cartwright S, Karakesisoglou I. 2014. Nesprins in health and disease. *Semin Cell Dev Biol* **29**:169–179. doi:10.1016/j.semcdb.2013.12.010

Chakouch MK, Pouletaut P, Charleux F, Bensamoun SF. 2016. Viscoelastic shear properties of in vivo thigh muscles measured by MR elastography. *J Magn Reson Imaging* **43**:1423–1433. doi:10.1002/jmri.25105

Chaudhury AR, Insolera R, Hwang R Der, Fridell YW, Collins C, Chronis N. 2017. On chip cryo-anesthesia of Drosophila larvae for high resolution in vivo imaging applications. *Lab Chip* **17**:2303–2322. doi:10.1039/c7lc00345e

Cho S, Irianto J, Discher DE. 2017. Mechanosensing by the nucleus : From pathways to scaling relationships 1–11.

Csordás G, Varga GIB, Honti V, Jankovics F, Kurucz É, Andó I. 2014. In vivo immunostaining of hemocyte compartments in Drosophila for live imaging. *PLoS One* **9**. doi:10.1371/journal.pone.0098191

Debernard L, Leclerc GE, Robert L, Charleux F, Bensamoun SF. 2013. in Vivo Characterization of the Muscle Viscoelasticity in Passive and Active Conditions Using Multifrequency Mr

Elastography . *J Musculoskelet Res* **16**:1350008. doi:10.1142/s0218957713500085

Dexter JP, Tamme MB, Lind CH, Collins EMS. 2014. On-chip immobilization of planarians for in vivo imaging. *Sci Rep* **4**:1–10. doi:10.1038/srep06388

Drost MR, Maenhout M, Willems PJB, Oomens CWJ, Baaijens FPT, Hesselink MKC. 2003. Spatial and temporal heterogeneity of superficial muscle strain during in situ fixed-end contractions. *J Biomech* **36**:1055–1063. doi:10.1016/S0021-9290(02)00461-X

Egan B, Zierath JR. 2013. Exercise metabolism and the molecular regulation of skeletal muscle adaptation. *Cell Metab* **17**:162–184.

Eldred CC, Simeonov DR, Koppes RA, Yang C, Corr DT, Swank DM. 2010. The mechanical properties of drosophila jump muscle expressing wild-type and embryonic myosin isoforms. *Biophys J* **98**:1218–1226. doi:10.1016/j.bpj.2009.11.051

Elhanany-Tamir H, Yu Y V., Shnayder M, Jain A, Welte M, Volk T. 2012. Organelle positioning in muscles requires cooperation between two KASH proteins and microtubules. *J Cell Biol* **198**:833–846. doi:10.1083/jcb.201204102

Elosegui-Artola A, Andreu I, Beedle AEM, Lezamiz A, Uroz M, Kosmalska AJ, Oria R, Kechagia JZ, Rico-Lastres P, Le Roux AL, Shanahan CM, Trepat X, Navajas D, Garcia-Manyes S, Roca-Cusachs P. 2017. Force Triggers YAP Nuclear Entry by Regulating Transport across Nuclear Pores. *Cell* **171**:1397-1410.e14. doi:10.1016/j.cell.2017.10.008

Fedorchak GR, Kaminski A, Lammerding J. 2014. Cellular mechanosensing: Getting to the nucleus of it all. *Prog Biophys Mol Biol* **115**:76–92. doi:10.1016/j.pbiomolbio.2014.06.009

Forgacs G, Newman SA. 2005. Biological physics of the developing embryo, Biological Physics of the Developing Embryo. doi:10.1017/CBO9780511755576

Fuks NA. 1964. The mechanics of aerosols. Oxford : Pergamon Press.

Gennisson JL, Deffieux T, Macé E, Montaldo G, Fink M, Tanter M. 2010. Viscoelastic and anisotropic mechanical properties of in vivo muscle tissue assessed by supersonic shear imaging. *Ultrasound Med Biol* **36**:789–801. doi:10.1016/j.ultrasmedbio.2010.02.013

Ghaemi R, Rezai P, Iyengar BG, Selvaganapathy PR. 2015. Microfluidic devices for imaging

neurological response of Drosophila melanogaster larva to auditory stimulus. *Lab Chip* **15**:1116–1122. doi:10.1039/c4lc01245c

Gupta RS. 2015. Elements of Numerical Analysis, second edi. ed. Cambridge University Press.

Hakim CH, Wasala NB, Duan D. 2013. Evaluation of Muscle Function of the Extensor Digitorum Longus Muscle Ex vivo and Tibialis Anterior Muscle In situ in Mice. *J Vis Exp* 1–8. doi:10.3791/50183

Hawley JA, Hargreaves M, Joyner MJ, Zierath JR. 2014. Integrative Biology of Exercise. *Cell* **159**. doi:10.1016/j.cell.2014.10.029

Hector AJ, McGlory C, Phillips SM. 2015. The influence of mechanical loading on skeletal muscle protein turnover. *Cell Mol Exerc Physiol* **4**. doi:10.7457/cmep.v4i1.e8

Hoyt K, Kneezel T, Castaneda B, Parker KJ. 2008. Quantitative sonoelastography for the in vivo assessment of skeletal muscle viscoelasticity. *Phys Med Biol* **53**:4063–4080. doi:10.1088/0031-9155/53/15/004

Janin A, Bauer D, Ratti F, Millat G, Méjat A. 2017. Nuclear envelopathies: A complex LINC between nuclear envelope and pathology. *Orphanet J Rare Dis* **12**:23–42. doi:10.1186/s13023-017-0698-x

Kakanj P, Eming SA, Partridge L, Leptin M. 2019. Long-term in vivo imaging of Drosophila larvae. *bioRxiv* 744383. doi:10.1101/744383

Kracklauer MP, Banks SML, Xie X, Wu Y, Fischer JA. 2007. Drosophila klaroid encodes a SUN domain protein required for klarsicht localization to the nuclear envelope and nuclear migration in the eye. *Fly (Austin)* **1**:75–85. doi:10.4161/fly.4254

Lombardi ML, Lammerding J. 2015. HHS Public Access **39**:1729–1734. doi:10.1042/BST20110686.Keeping

Martins RP, Finan JD, Farshid G, Lee DA. 2012. Mechanical Regulation of Nuclear Structure and Function. *Annu Rev Biomed Eng* **14**:431–455. doi:10.1146/annurev-bioeng-071910-124638

Méjat A, Misteli T. 2010. LINC complexes in health and disease. *Nucleus* **1**:40–52.

doi:10.4161/nucl.1.1.10530

Mellad JA, Warren DT, Shanahan CM. 2011a. Nesprins LINC the nucleus and cytoskeleton. *Curr Opin Cell Biol* **23**:47–54. doi:10.1016/j.ceb.2010.11.006

Mellad JA, Warren DT, Shanahan CM. 2011b. Nesprins LINC the nucleus and cytoskeleton. *Curr Opin Cell Biol* **23**:47–54. doi:10.1016/j.ceb.2010.11.006

Miroshnikova YA, Nava MM, Wickström SA. 2017. Emerging roles of mechanical forces in chromatin regulation. *J Cell Sci* **130**:2243–2250. doi:10.1242/jcs.202192

Mondal S, Ahlawat S, Koushika SP. 2012. Simple Microfluidic Devices for in vivo Imaging of C. elegans, Drosophila and Zebrafish. *J Vis Exp* 1–9. doi:10.3791/3780

Olatunji O. 2015. Natural Polymers: Industry Techniques and Applications.

Osmanagic-Myers S, Dechat T, Foisner R. 2015. Lamins at the crossroads of mechanosignaling. *Genes Dev* **29**:225–237. doi:10.1101/gad.255968.114

Puckelwartz MJ, Kessler EJ, Kim G, DeWitt MM, Zhang Y, Earley JU, Depreux FFS, Holaska J, Mewborn SK, Pytel P, McNally EM. 2010. Nesprin-1 mutations in human and murine cardiomyopathy Megan. *J Mol Cell Cardiol* **48**:600–608. doi:10.1016/j.yjmcc.2009.11.006

Rajgor D, Shanahan CM. 2013. Nesprins: from the nuclear envelope and beyond. *Expert Rev Mol Med* **15**:e5. doi:10.1017/erm.2013.6

Rindom E, Vissing K. 2016. Mechanosensitive molecular networks involved in transducing resistance exercise-signals into muscle protein accretion. *Front Physiol* **7**:1–9. doi:10.3389/fphys.2016.00547

Rothballer A, Kutay U. 2013. The diverse functional LINCs of the nuclear envelope to the cytoskeleton and chromatin. *Chromosoma* **122**:415–429. doi:10.1007/s00412-013-0417-x

Sloboda DD, Claflin DR, Dowling JJ, Brooks S V. 2013. Force Measurement During Contraction to Assess Muscle Function in Zebrafish Larvae. *J Vis Exp* 1–10. doi:10.3791/50539

Stroud MJ, Feng W, Zhang J, Veevers J, Fang X, Gerace L, Chen J. 2017. Nesprin 1α2 is

essential for mouse postnatal viability and nuclear positioning in skeletal muscle. *J Cell Biol* **216**:1915–1924. doi:10.1083/jcb.201612128

Uhler C, Shivashankar G V. 2017. Regulation of genome organization. *Nat Publ Gr* **18**:717–727. doi:10.1038/nrm.2017.101

Wan LQ, Jiang J, Arnold DE, Guo XE, Lu HH, Mow VC. 2009. NIH Public Access **1**:93–102. doi:10.1007/s12195-008-0014-x.Calcium

Wang S, Reuveny A, Volk T. 2015. Nesprin provides elastic properties to muscle nuclei by cooperating with spectraplakin and EB1. *J Cell Biol* **209**:529–538. doi:10.1083/jcb.201408098

Wang S, Stoops E, Unnikannan CP, Markus B, Reuveny A, Ordan E, Volk T. 2018. Mechanotransduction via the LINC complex regulates DNA replication in myonuclei. *J Cell Biol* **217**:2005–2018. doi:10.1083/jcb.201708137

Webster JG, Eren H, editors. 2018. Measurement, Instrumentation, and Sensors Handbook: Two-Volume Set, second. ed. CRC Press.

Wolf S, Supatto W, Debrégeas G, Mahou P, Kruglik SG, Sintes JM, Beaurepaire E, Candelier R. 2015. Whole-brain functional imaging with two-photon light-sheet microscopy. *Nat Methods* **12**:379–380. doi:10.1038/nmeth.3371

Xie X, Fischer JA. 2008. On the roles of the Drosophila KASH domain proteins Msp-300 and Klarsicht. *Fly (Austin)* **2**:74–81. doi:10.4161/fly.6108

Zhang Q, Bethmann C, Worth NF, Davies JD, Wasner C, Feuer A, Ragnauth CD, Yi Q, Mellad JA, Warren DT, Wheeler MA, Ellis JA, Skepper JN, Vorgerd M, Schlotter-Weigel B, Weissberg PL, Roberts RG, Wehnert M, Shanahan CM. 2007. Nesprin-1 and -2 are involved in the pathogenesis of Emery - Dreifuss muscular dystrophy and are critical for nuclear envelope integrity. *Hum Mol Genet* **16**:2816–2833. doi:10.1093/hmg/ddm238

Zhang Q, Ragnauth C, Greener MJ, Shanahan CM, Roberts RG. 2002. The nesprins are giant actin-binding proteins, orthologous to Drosophila melanogaster muscle protein MSP-300. *Genomics* **80**:473–481. doi:10.1016/S0888-7543(02)96859-X

Zhang W, Sobolevski A, Li B, Rao Y, Liu X. 2016. An Automated Force-Controlled Robotic Micromanipulation System for Mechanotransduction Studies of Drosophila Larvae. *IEEE Trans Autom Sci Eng* **13**:789–797. doi:10.1109/TASE.2015.2403393

Zhang Y, Füger P, Hannan SB, Kern J V., Lasky B, Rasse TM. 2010. In vivo Imaging of Intact Drosophila Larvae at Sub-cellular Resolution. *J Vis Exp* 4–7. doi:10.3791/2249

Figure legends

Figure 1: The minimal constraint device for imaging live intact *Drosophila* larvae

(A) Configuration of the device, lens perspective: The larva is placed along a groove with two glass capillaries filled with glue attached to its head and tail. The space between the larva and plastic bar is filled with hydrogel. B) The larva attached to the glass capillaries in the Delrin bar.

Top view: A glass coverslip is laced in the device base and secured to its place by four rubber stoppers. The frame and the bar with the larva are placed on top of the glass. The hinge attached to the frame assures its right positioning;

Figure 2: Measurements of nuclear displacement and parameters calculations

(A) An example of two sequential images of contractile muscle demonstrating myonuclear displacement of 5 nuclei during a time interval of 82 ms (red is t=0 and green is t=82 ms). (B) The displacement in time of a single nucleus during a complete contraction. (C) The velocity of a nucleus during contraction was calculated based on the temporal displacement function. (D) The acceleration of a nucleus during contraction was calculated based on the displacement function.

Figure 3: Detection of myonuclei during contraction

(A-D) Control (A,-D) and *Nesprin*/*klar* mutant (E-H) myonuclei labeled with Cherry-NLS driven by *Mef2-GAL4* in relaxed (A, B, E, F) or fully contractile (C, D, G, H) muscles. Sarcomeres are labeled with Sls-GFP. Scale bars are 20 μm.

Figure 4: The path of the nuclei during contraction

(A) The path that each of the control myonuclei (nuc) shown in Figure 3A, C, E, G undertakes during a full contractile event. (B) The path that each of the *Nesprin/klar* myonuclei shown in Figure 3B, D, F, E undertakes during a full contractile event.

Figure 5: Quantification of nuclear mechanical parameters in control and *Nesprin*/*klar* larvae during muscle contractile waves

The average contractile time (milliseconds, ms) in *klar* and control myonuclei. Each point represents the average of 6 to 10 contractile events per larvae in all panels (as detailed in Table 1

and Figure 3). The averaged contraction time for control was 1286.32 ± 371.55 ms and for *klar* mutant 715.16 ± 245.68 ms (*t*-test, p=0.0024). (B) The average path during a single contractile event of all the nuclei measured per larvae. The average path was 50.64 ± 9.93 μm for control and 29.1 ± 5.43 μm for *klar* mutants (*t*-test, p=0.005). In each muscle there were 6 to 17 nuclei, thus each point represents 42 to 130 measurements. (C) The average velocity of myonuclei per individual contractile event. No significant difference was observed. (D) The average velocity of anterior, middle, or posterior myonuclei. A significant difference between the average velocity of posterior myonuclei between *klar* mutants and control larvae was observed (p=0.012). (E) The average acceleration values of myonuclei in *klar* mutants ($-1.39\cdot10^{-4}\pm7.8\cdot10^{-5}$ μm/msec^2) and control larvae ($3.14\cdot10^{-5}\pm2.42\cdot10^{-5}$ μm/msec^2) (p=0.034). The variance of the average acceleration was significantly higher in *klar* mutants versus control (p=0.044). (F) Average acceleration values calculated per anterior, middle, or posterior myonuclei. A significant difference was observed between control and *klar* mutant myonuclei at the posterior position (p=0.009).

Figure 6: The dependency of myonuclear volume and average acceleration, reveals opposite trends between *klar* mutant muscles and control

Plot of myonuclear volume against the average acceleration values of each nucleus of control (upper panel) or Nesprin/klar mutant muscles (lower panel). Note the opposite tendencies in the graphs of the two groups (interaction p= 0.007).

Figure 7: Estimation of the drag force applied on myonuclei during contraction and its link to myonuclear volume

(A) The average drag force values for control and *Nesprin*/*klar* mutants do not differ (p=0.73). (B) The absolute average force time derivative (AFDT) during contraction is significantly higher in *Nesprin*/*klar* versus control myonuclei (p=0.033) with an order of magnitude higher variance (p=0.048). (C) AFTD values differed along the myofiber in *Nesprin*/*klar* mutant muscles (p=0.00165), whereas control myonuclei displayed uniformity along the myofiber (p=0.3).

(D) Plot of myonuclear volume against the AFTD values of each nucleus of control (upper panel) or *Nesprin/klar* mutant muscles (lower panel). Note the opposite tendencies in the graphs of the two groups (interaction p= p=0.029).

Lorber et al, Figure 1

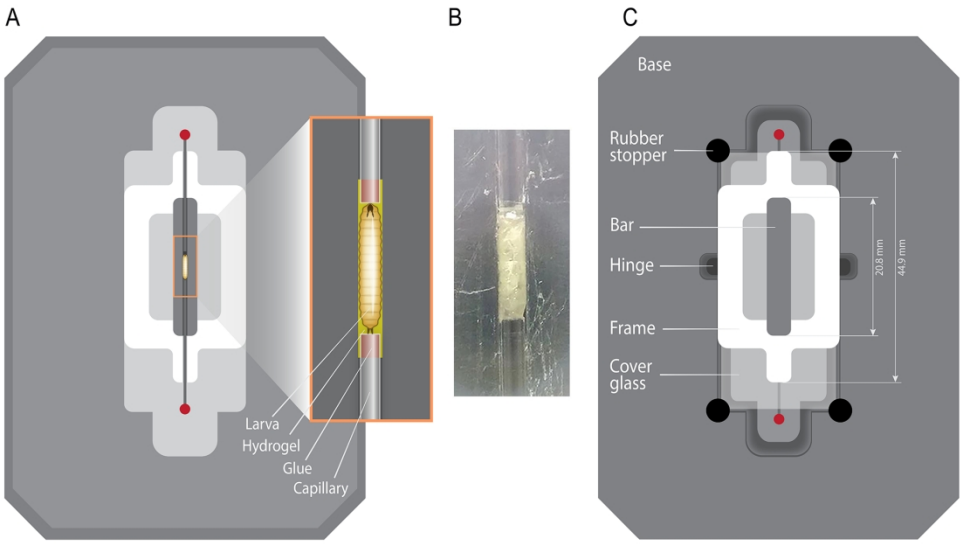

Figure 1

Lorber et al., Figure 2

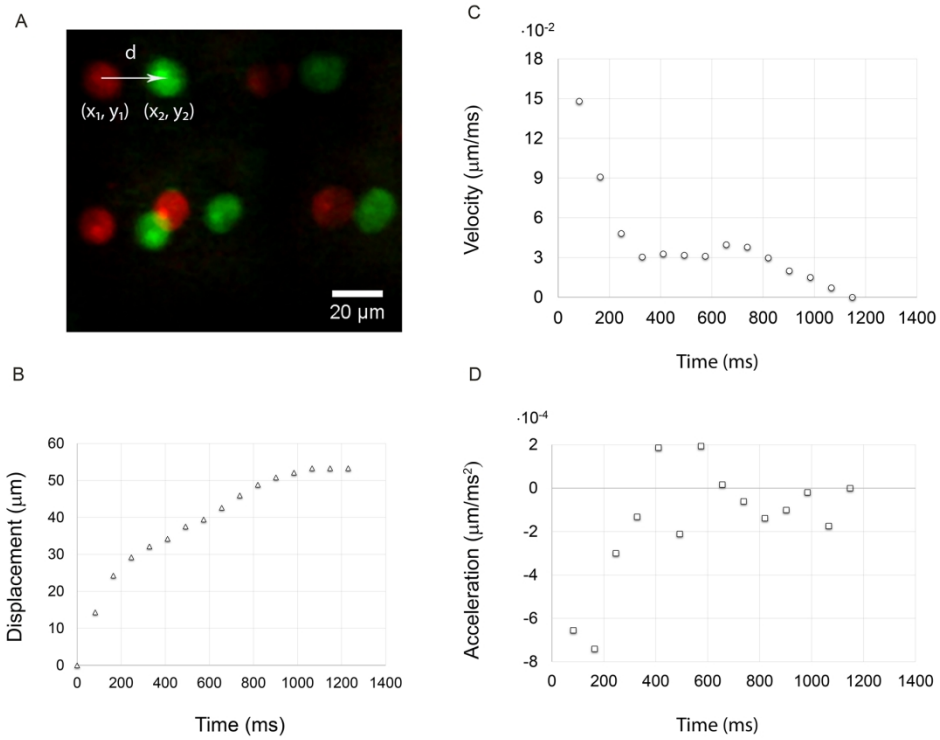

Figure 2

Lorber et al., Figure 3

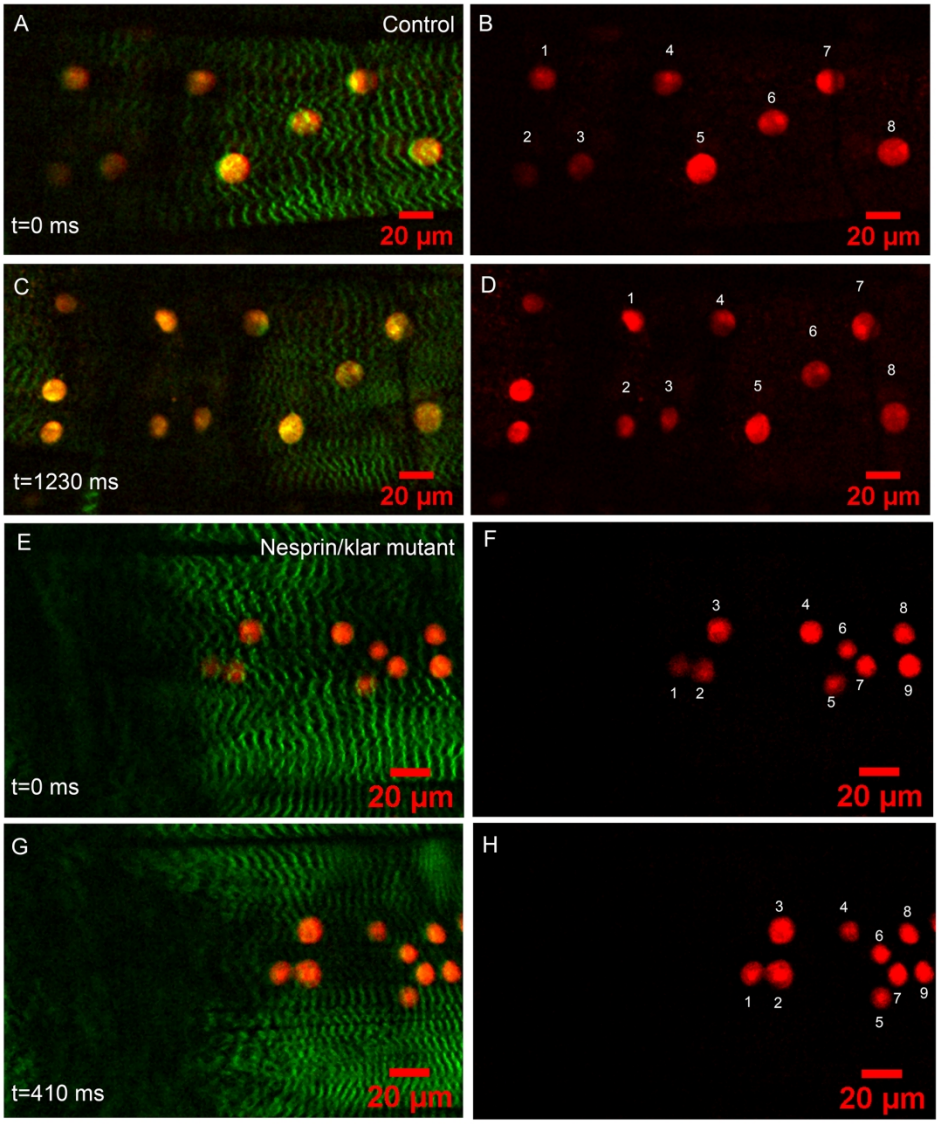

Figure 3

Lorber et al., Figure 4

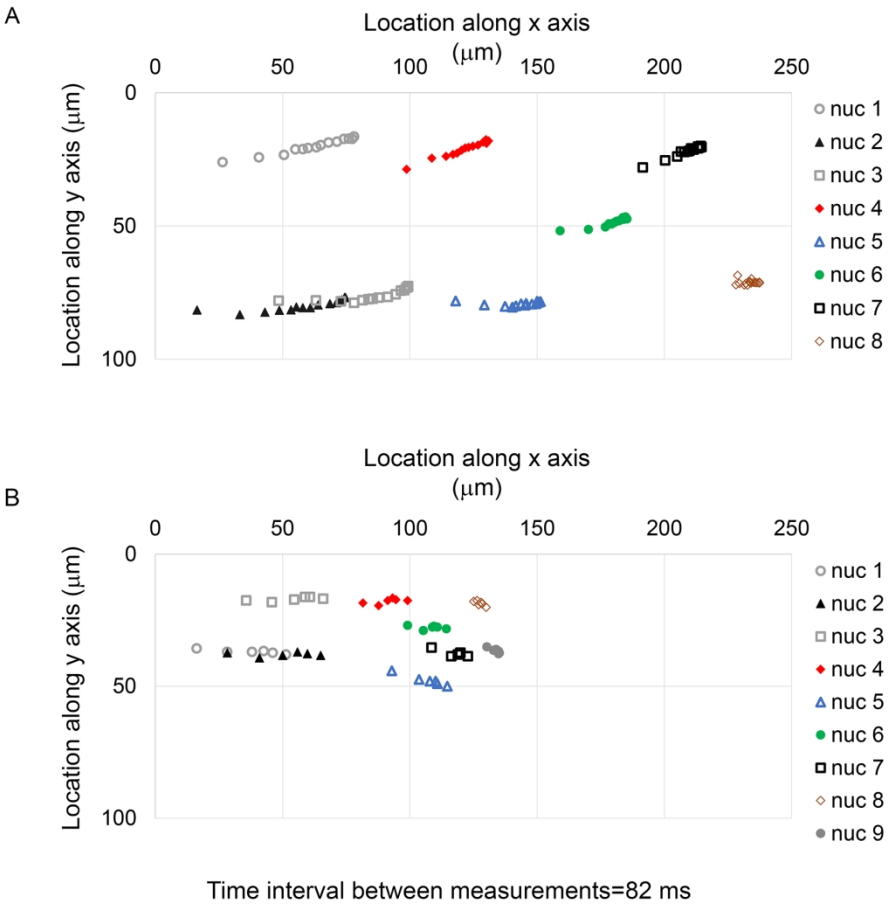

Figure 4

Lorber et al., Figure 5

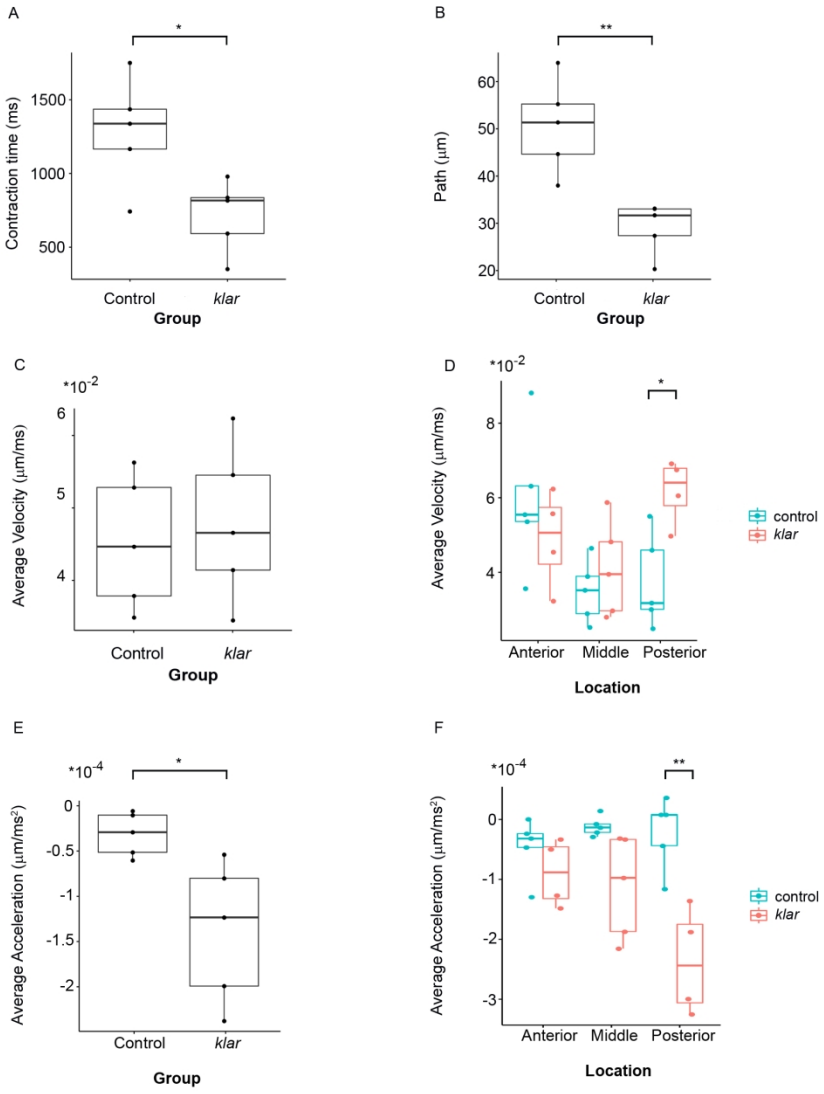

Figure 5

Lorber et al., Figure 6

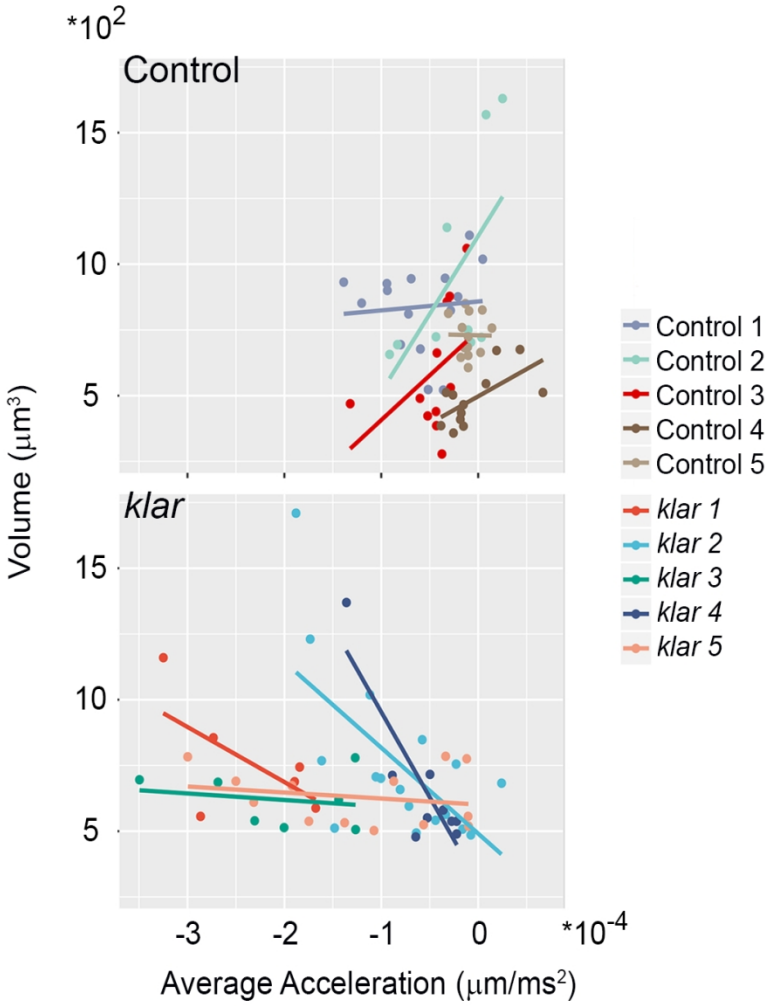

Figure 6

Lorber et al., Figure 7

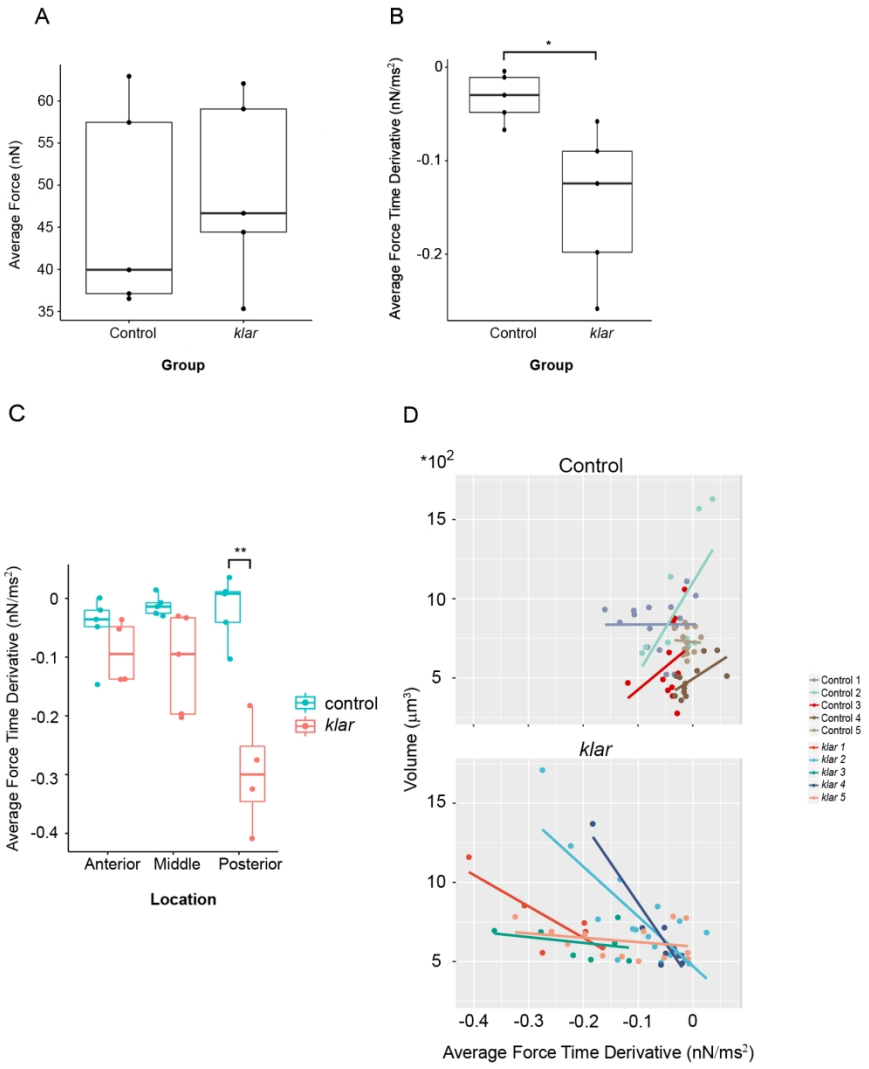

Figure 7